https://doi.org/10.15407/ufm.24.04.819

G.S. FIRSTOV[1,*], Yu.M. KOVAL[1], V.S. FILATOVA[1], V.V. ODNOSUM[1], G. GERSTEIN[2], and H.J. MAIER[2]

[1] G.V. Kurdyumov Institute for Metal Physics of the N.A.S. of Ukraine, 36 Academician Vernadsky Blvd., UA-03142 Kyiv, Ukraine

[2] Institut für Werkstoffkunde Leibniz Universität Hannover, An der Universität 2, D-30823 Garbsen, Germany

* yuri.firstov@gmail.com

DEVELOPMENT OF HIGH-ENTROPY SHAPE-MEMORY ALLOYS: STRUCTURE AND PROPERTIES

Amongst functional materials, shape-memory alloys occupy a special position. After their discovery these alloys attracted substantial attention because of the possibility to restore significant deformation amounts under certain stress–temperature conditions due to the martensitic diffusionless phase transformation involved. It was possible to exploit not only so-called 'shape-memory' effect, but also superelasticity and high damping capacity. Over the years, more than 10 000 patents on shape-memory alloys were filed, appreciating not only the possibility to exploit the energy transformation to ensure the response (feedback) at the change in independent thermodynamic parameters (temperature, stress, pressure, electric or magnetic field, *etc.*), but the significant work output as well. The envisaged shape memory components covered applications in the automotive, aerospace, machine building and civil construction industries. Unfortunately, structural and functional fatigue restricted successful business application mostly to the medical sector, with the Nitinol shape-memory alloy dominating applications such as different implants, stents or cardiovascular valves. Emerging high-entropy shape-memory alloys can be considered as a chance to overcome the fatigue problems of today's shape-memory alloys due to their specific structure that ensures superior resistance to irreversible plastic deformation.

Keywords: high-entropy shape-memory alloys, martensitic transformation, structure, multiple principal element intermetallic compounds, mechanical properties, shape memory and related phenomena.

Citation: G.S. Firstov, Yu.M. Koval, V.S. Filatova, V.V. Odnosum, G. Gerstein, and H.J. Maier, Development of High-Entropy Shape-Memory Alloys: Structure and Properties, *Progress in Physics of Metals*, **24**, No. 4: 819–837 (2023)

1. Introduction

Over the last two decades the high-entropy alloys (HEA) were introduced as novel class of structural materials [1]. The HEA concept involves the creation of multi-element metallic materials close to an equimolar composition, *i.e.*, without a principal element. The entropy of mixing is higher compared to conventional materials and promotes a high phase stability [2–6]. HEA are also known for their non-obvious solution hardening [7, 8]. In parallel, in the field of functional shape memory alloys design, the pursuit of the so-called high-temperature shape memory alloys has taken place with the obvious difficulties regarding functional degradation at elevated temperatures associated with the movement of full dislocations [9–13]. The application of the high entropy concept to shape memory alloys using NiTi as a prototype resulted in a first successful attempt in the TiZrHfCoNiCu alloy system with a martensitic transformation accompanied by a shape memory effect in a wide temperature range. Reversible deformation of about 2% was obtained with the suppression of all the fatigue effects mentioned in [9–13] due to the two-fold increase in yield strength ensured by the multi-component design. In this way, a novel class of functional materials has been introduced, termed high-entropy shape-memory alloys (HESMA) [14, 15]. Later, additional HESMA systems were proposed. Some of them were generated following the idea of the NiTi prototype used in multi-component design [14, 15], while in other cases it was tried to obtain solid solutions of a different kind.

The authors of [16] reviewed all HESMAs in general and grouped them as 'NiTi-like', 'Fe-like', 'Ti-based' and others that are belonging to those that tend to exhibit magnetic shape memory. Still, they viewed the design criteria for HESMA as rather empirical ones. It should be noted that the 'Fe-like' and 'Ti-based' solid solutions described in [16] are mostly multi-component (starting from only 4 constituents) alloys with medium entropy of mixing just bordering the high entropy range because of the emerging principal element contrary to the often overlooked part of J.W. Jeh's concept [1] that includes the notion of multiple principal elements.

It is not just a mere technicality that HEAs in general can not be based upon one, two, and, probably, even three elements. High entropy of mixing (ΔS_{mix}) in HESMAs is not a goal but a reflection of the useful structural states formation (lattice distortion, cocktail effect, ...). Here one needs a good balance of the lattice distortion effect that results in mechanical properties superior to shape memory alloys based upon Fe, NiTi, Ti and phase stability of the austenite. Specifically diffusional transformations need to be suppressed, while martensitic diffusionless phase transformation has to be possible. The latter takes place because the high entropy of mixing indeed complicates diffusion driven phase

transformations due to the necessity to change chemical composition, while martensite transformation is diffusionless, thus the chemical composition remains unchanged and, therefore, there is no influence of the high entropy of mixing in this case.

So far, the solid solutions claimed as HESMAs are not quite fitting into the reasoning regarding principal elements and lattice distortion mentioned above. For instance, in [17] the authors claim a strategy of designing high-entropy alloys with high-temperature shape memory effect in terms of relative stability between f.c.c. (austenite) and h.c.p. (martensite) crystal structures that ended up with the $Cr_{20}Mn_{20}Fe_{20}Co_{35}Ni_5$ alloy, which exhibited an f.c.c. to h.c.p. martensitic transformation (MT) because the emerging principal element in this case was Co known to exhibit this type of MT. Almost 2% of shape memory accompanied heating of the $Cr_{20}Mn_{20}Fe_{20}Co_{35}Ni_5$ alloy pre-strained up to 7.6% (*i.e.*, the shape recovery ratio is 24% only). Such shape recovery cannot be considered sufficient. Obviously, in this case the benefits of the multiple principal element design (lattice distortions mentioned above as reflected in atomic size difference δ — one of the parameters characterising collective behaviour of HEA constituents [18]) visible in the stable f.c.c. Cantor alloy with the equiatomic CrMnFeCoNi composition (ΔS_{mix} = = 13.381 $Jmol^{-1}K^{-1}$, δ = 3.269%) were lost for the Co-based $Cr_{20}Mn_{20}Fe_{20}Co_{35}Ni_5$ alloy (ΔS_{mix} = 12.329 $Jmol^{-1}K^{-1}$, δ = 3.239%). In the latter, irreversible plastic deformation overwhelmed the martensitic recoverable one generally due to the decrease in δ (lattice distortion), and the entropy of mixing is decreasing too. Similar effects to $Cr_{20}Mn_{20}Fe_{20}Co_{35}Ni_5$ but with much better functional behaviour were seen in the Fe–Mn–Si system. Its development has started in the early 80s of the last century [19] and is still ongoing (see [20, 21], for example). So-called Fe-based HESMA defined as such in [22] are very similar to the Fe–Mn–Si-based shape memory alloys mentioned above and their development is not based on the high entropy or multiple principal element design. Moreover, for $Ti_{49\div50}Zr_{20}Hf_{15}Al_{10}Nb_{5\div6}$ shape memory alloy mentioned as a 'high entropy', ΔS_{mix} = 11.08 to 11.26 $Jmol^{-1}K^{-1}$ and complete superelasticity does not exceed 2 to 3% [23], while for the Ti-based $Ti_{68}Zr_{18}Nb_{11}Sn_3$ superelastic alloy [24] (ΔS_{mix} = 10.316 $Jmol^{-1}K^{-1}$) 500 cycles with a reversible strain of almost 5% were realised. It seems like in the case of the multiple principal element solid solution shape memory alloys (medium or high entropy) the increase in yield strength might not be enough for preventing plastic deformation that accompanies the recoverable martensitic one, while slightly modified ternary composition with one principal element might work because of reasons related to crystal structure and microstructural peculiarities.

The first HESMA developed [14–15] and the alloys similar to them termed 'NiTi-like' in [16] are, in fact, multi-element intermetallic com-

pounds. The peculiar structure of these intermetallics [25] ensured by the multiple principal element design was indeed the reason for their superior functional properties compared to the ones of solid solution HEA with MT or industrial shape memory alloys. Therefore, the present paper focuses on important development directions of these high entropy multi-element based *B*2 type intermetallic materials.

2. Crystal Structure Design of the *B*2-Type Multi-Element-Based Intermetallics Undergoing Martensitic Transformation

Speaking of intermetallic compounds and structure prototypes, most known are binary and ternary ones [26]. It has to be noted that the HEA design was always focused on solid solutions and amorphous phases (*cf*. [18, 27]) due to the effect of high configurational entropy of mixing although formation of intermetallic phases in HEA was duly recognised [3, 18, 27, 28] leading eventually to the recognition of high-entropy intermetallics (HEI) in general [29]. In Ref. [6], the formation of single *C*14 Laves phase of equiatomic composition was reported despite the fact that it contained 26 (!) constituents with an extremely high ΔS_{mix} of 28.131 $Jmol^{-1}K^{-1}$. It seems that the entropy of mixing does not play the key role in formation of HEI. According to [27], phase selection for HEI is governed by the enthalpy of mixing and the atomic size difference (see Fig. 1 of [27]). Meanwhile, the entropy of mixing reflects the random mixing appearing on sublattices of certain intermetallic compounds like *B*2 ones that possess two of those sublattices.

The *B*2 type (CsCl structure type) is quite characteristic of the high temperature austenitic phase for shape memory alloys in general and high temperature shape memory alloys in particular [13]. In this regard, not only NiTi can be taken as a prototype for HEA with the *B*2 structure. For the TiZrHfCoNiCu system in addition to the stable TiCo, ZrCo, HfCo, ZrNi, TiCu, HfCu, binary *B*2 compounds exist that undergo a MT also, namely, HfNi and ZrCu. The latter is known as a high temperature shape memory alloy itself [30, 31]. The equiatomic TiZrHf CoNiCu possesses a valence electron concentration identical to NiTi and it was expected to obtain not only *B*2 structure for austenite but a MT with a product similar to NiTi. X-ray diffraction results from [14] clearly show that as-cast equiatomic TiZrHfCoNiCu exhibits qualitatively a pattern of the *B*2 type in addition to b.c.c. reflections. The (100) peak was clearly seen (evidence of the sublattices formation) without any peaks for a martensitic phase. At the same time, those reflections appeared to be shifted from the expected *B*2 positions in different directions indicating that a lower symmetry might be taken place for the observed structure.

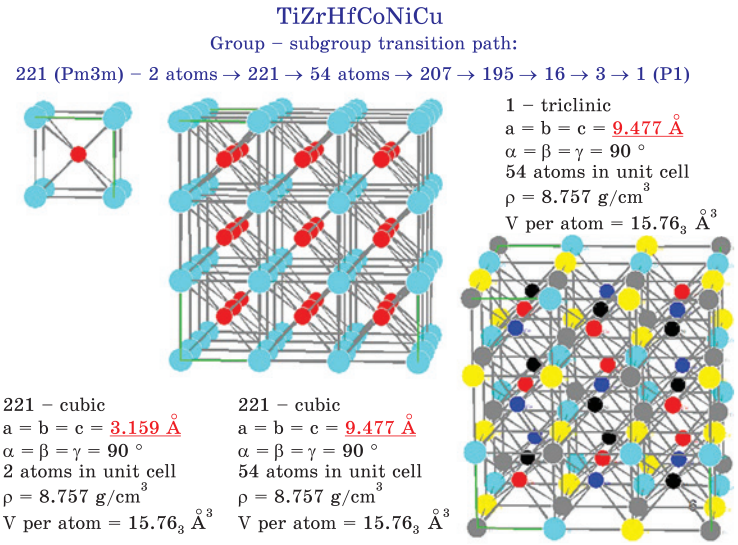

Fig. 1. Triclinic (*P*1, No. 1) ideal unit cell of the TiZrHfCoNiCu HEA ($a_{P1} = b_{P1} = c_{P1} = 9.477$ Å and $\alpha_{P1} = \beta_{P1} = \gamma_{P1} = 90°$) derived from the *B*2 (*Pm*3*m*, No. 221) unit cell ($a_{B2} = 3.159$ Å) through the following group–subgroup transition path: No. 221 (*Pm*3*m*; 2 atoms) → 221 (54 atoms) → 207 → 195 → 16 → 3 → No. 1 (*P*1) [25, 32]

In addition to the mentioned indications, there was a problem of fitting 6 types of atoms into *B*2 unit cell. A chaotic distribution of the Ti, Zr, Hf atoms at 1a Wyckoff position and Co, Ni, Cu — at 1b Wyckoff position (or vice versa) was definitely a possibility to simplify the situation (which was mostly done by all the authors that performed XRD data analysis on these multi-component intermetallics). Still, there is a way to obtain a unit cell with all 6 types of atoms occupying own Wyckoff positions as it was briefly shown in [25]. To do that, the group-subgroup transition shown in Fig. 1 was applied to the *B*2 structure (space group 221, *Pm*3*m*) with the lattice parameter experimentally obtained on an as-cast TiZrHfCoNiCu compound in [14] ($a_{B2} = 3.159_0$ Å, volume per atom 15.763 Å^3).

It was found that only in the case of space group 1, *P*1 there is a possibility to accommodate all 6 types of atoms. There redistribution onto sublattices [32] was done with the help of a special quasi-random structure method and ab-initio modelling was performed with subsequent verification with a Rietveld refinement of the x-ray diffraction data (Maud software [33]). The results are shown in Figs. 2 and 3. It is shown in Fig. 2 that in the homogenised state equiatomic TiZrHfCoNiCu exhibits a single phase with a crystal structure that corresponds to the modelling results well. It belongs to the triclinic syngony and its

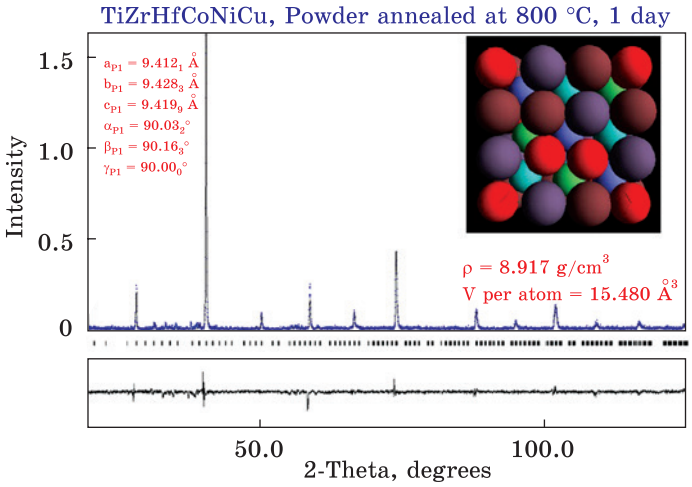

Fig. 2. Results of the Rietveld refinement (Maud software [33]) of x-ray data obtained with CuK_α radiation on equiatomic TiZrHfCoNiCu powder annealed at 800 °C for 1 day [32]

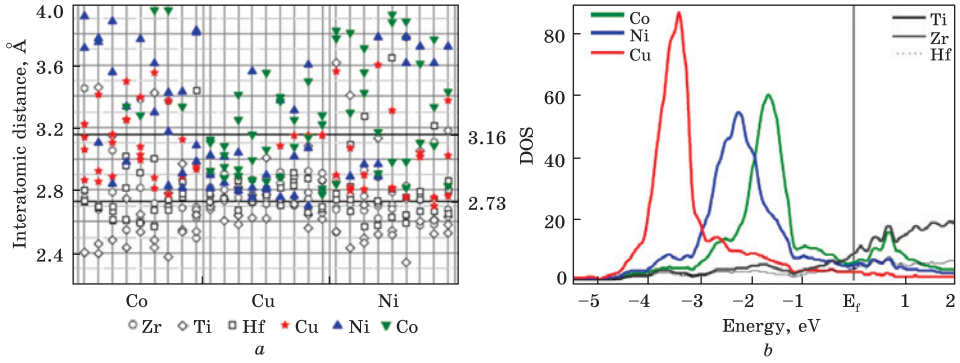

Fig. 3. a — Calculated interatomic distances of *A*–*B* and *B*–*B* (*A* = Ti, Zr, Hf; *B* = Co, Ni, Cu) types in the model $Ti_9Zr_9Hf_9Co_9Ni_9Cu_9$ structure (interatomic distances in the ideal structure prior to optimization (Fig. 1) *A*–*B* = 2.73 Å and *B*–*B* = 3.16 Å are also shown); *b* — local electron densities of states (DOS) of atoms in the model $Ti_9Zr_9Hf_9Co_9Ni_9Cu_9$ structure [25, 32]

density is higher (volume per atom smaller) compared to the oversimplified *B*2 variant shown in Fig. 1.

Figure 3, *a* shows bond lengths for Co, Cu and Ni atoms. It can be seen that the bond lengths between Cu and Ti, Zr and Hf atoms are close to ideal ones but the bond lengths between Co, Ni and Ti, Zr, Hf atoms are significantly smaller than in the ideal (2.73 Å) case. It should be also noted that the interatomic distances between Cu, Ni and the other Co, Cu and Ni atoms are also significantly smaller than the ideal ones. In other words, it means that some Cu and Ni atoms are entering the first coordination sphere for other Ni and Cu atoms. Co interacts in a strong manner with *A* atoms (*A* = Ti, Zr, Hf) but Cu atoms are the closest to Co ones amongst the atoms of *B* type (*B* = Cu, Ni, Co). This might help to

explain why Ni replacement by Co is accompanied by stronger densification of the structure and a more intensive decrease in the MT transformation temperatures. While Co atoms replace Ni ones, Co–Cu and Co–(Ti, Zr, Hf) interactions increase as the bond length distribution in Fig. 3, *a* suggests. This will definitely stabilize the high temperature austenitic phase against the MT and the volume per atom will decrease. As for the Cu replacement and the mutual replacement effects of Cu and Ni by Co on the MT, further experimental and modelling studies are needed. These should not employ the $B2$ and $B19'$ crystal structures but the triclinically distorted $B2$ austenite phase and, consequently, a much needed triclinic model of the distorted $B19'$ martensite phase.

All the crystal structure peculiarities of the triclinic TiZrHfCoNiCu high temperature phase (Fig. 2, 3, *a*) as compared to the initial triclinic model in Fig. 1 are a direct consequence of electronic structure shown in Fig. 3, *b*. It is visible (Fig. 3, *b*) that the occupied part of the density of electronic states (DOS) is formed by *d*-zones of Cu, Ni and Co atoms. Non-occupied states are caused by Ti, Zr, and Hf atoms. Electronic structure analysis has shown that *d*-states of Cu and Ni are hybridized stronger than the Cu and Co ones. This is due to the fact that the DOS peaks of Cu and Ni are close to each other. The electronic states of Co are more hybridized with the electronic states of Ti, Zr and Hf atoms, compared with Cu and Ni atoms. Hybridization effects are the reason for the formation of interatomic bond lengths in the model structure, that were described above. Thus, it is possible to conclude that Co atoms in high-entropy intermetallics of TiZrHfCoNiCu family promote the stabilization of the high temperature austenitic triclinically distorted $B2$ phase, while Cu and Ni atoms lead to its structural instability.

In fact, the findings described above remind one of the results related to the origin of the MT in ZrCu [13, 34, 35]. There, the origin of the austenitic phase instability was found in the possibility of the existence of two types with short-range order. The first short range order type is determined by the Cu–Zr interaction, while the second by the Cu–Cu one. Later, the same situation was noticed for the TiNi intermetallic compound [13]. In both cases, Cu–Zr or Ni–Ti interatomic interaction stabilizes the high temperature $B2$ phase, while Cu–Cu or Ni–Ni ones appear in the martensitic phases. This was clearly seen for martensitic crystal structures by the appearance of Cu (Ni) atoms in the first coordination sphere of the atoms of their own sort [13, 34, 35].

In the present case of the $(TiZrHf)_{50}(CoNiCu)_{50}$ high-entropy intermetallic compound, the same effect of the appearance of Cu and Ni atoms in the first coordination sphere of the atoms of their own sort is clearly visible in the high temperature austenitic phase (Fig. 3, *b*). It shows that the parent phase crystal structure is distorted already in such a way that it seems even better prepared for the possible MT than

in the binary ZrCu or TiNi intermetallic compounds because their austenitic structures are dominated by only one sort of interatomic interaction. These distortions in the crystal structure of the high-entropy intermetallic compound resulted in a triclinic structure, which is possible due to higher number of degrees of freedom given by the multi-element composition. In addition, the authors of [36] independently obtained results about the triclinic structure of quaternary and quinary equiatomic refractory solid solution high-entropy alloys that become an extra confirmation for a tendency of low symmetry structure formation in alloys prepared with the help of the multiple principal element design. At the same time, the mere fact of a triclinic structure of the austenite phase might help to explain quite a few facts like the absence of MT in equiatomic TiZr HfCoNiCu despite the valence electron concentration and better preparedness for the MT and the significant strengthening in addition to the obvious lattice distortion effect. In case of the triclinic structure, one might expect difficulties with the martensite nucleation. As for the strengthening, it is literally quite difficult to define the slip system in such a lattice.

It can be concluded that in the high entropy TiZrHfCoNiCu intermetallic compounds two types of interatomic interaction of A–B and B–B type (A = Ti, Zr, Hf; B = Co, Ni, Cu) can be considered in general as the reason for the structural instability towards the martensitic transformation. Such instability as well as plastic deformation is controlled by the triclinically distorted lattice within the TiZrHfCoNiCu system.

It should be noted that the multiple principal element structural design described in this section was successfully applied to the case of CoNiCuAlGaIn HEI that exhibited a $B2 \leftrightarrow L1_0$ MT [37]. In fact, the formation of low-symmetry distorted $B2$ high-entropy intermetallics undergoing a MT seems to be becoming a physical regularity. In the following, it is considered how the described structural design might influence phase formation, properties and microstructure within the TiZrHfCoNiCu system.

3. Phase Formation, Some Properties and Microstructure within TiZrHfCoNiCu System

The work in [38] represents an attempt to describe the changes in structure, phase formation and properties in the as-cast state while moving from equiatomic TiZrHf to the TiZrHfCoNiCu ternary system through Co, Ni and Cu additions. As a result, a room temperature non-equilibrium ternary phase diagram was obtained. In Figure 4, the concentrations for Ti, Zr and Hf are identical and equal to 16.667 at.% for the whole diagram. This diagram was chosen on a basis of the findings related to the electronic and crystal structure of the TiZrHfCoNiCu HEI described in the previous section. It was shown that the strong interac-

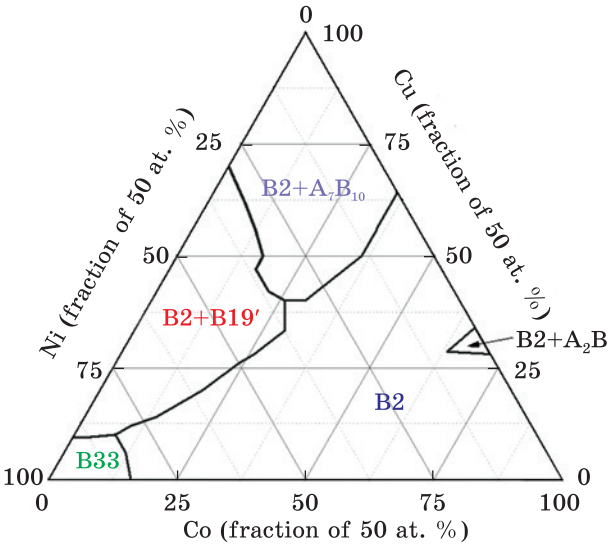

Fig. 4. As-cast room temperature non-equilibrium ternary phase diagram for $Ti_{16.67}Zr_{16.67}Hf_{16.67}Co_{0÷50}Ni_{0÷50}Cu_{0÷50}$ system [38] (A = Ti, Zr, Hf; B = Co, Ni, Cu)

tion between A atoms (Ti, Zr, Hf) and B atoms (Co, Ni, Cu) is responsible for the $B2$ structure stability, while the B–B interaction governs the instability. Thus, it makes sense to look at such a phase diagram in terms of the B atoms concentration. It can be clearly seen that the $B2$ phase (here the oversimplified $B2$ structure is used for clarity) definitely dominates the diagram and is observed as a single phase in a wide range from the Co rich corner bordering a small area occupied by a single $B33$ orthorhombic phase around the Ni rich corner. It also borders an area around the Cu rich corner occupied by the $B2$ and A_7B_{10} phase. Between the areas of the single $B2$, single $B33$ and ($B2$ + A_7B_{10}) phases (A = Ti, Zr, Hf; B = Co, Ni, Cu) lies the area where the $B2$ high temperature austenitic phase coexists with the $B19'$ phase, which is a product of the martensitic transformation. There is also a small pocket of coexisting $B2$ and A_2B phases around the $Ti_{16.67}Zr_{16.67}Hf_{16.67}Co_{35}Cu_{15}$ composition. It has to be noted that most phases are HEI with a maximal ΔS_{mix} of 14.897 J mol^{-1}K^{-1} for equiatomic TiZrHfCoNiCu, while at the corners, the $Ti_{16.67}Zr_{16.67}Hf_{16.67}Co_{50}$, $Ti_{16.67}Zr_{16.67}Hf_{16.67}Cu_{50}$ and $Ti_{16.67}Zr_{16.67}Hf_{16.67}Ni_{50}$ compositions can be considered as medium entropy because for them ΔS_{mix} = 10.33 Jmol^{-1}K^{-1}. The A_2B phase can be based upon two different types, *i.e.* Ti_2Ni ($Fd3m$) or Hf_2Ni ($I4/mcm$). The A_7B_{10} phase is based upon Zr_7Ni_{10} ($Cmca$). $B33$ is an orthorhombic phase (CrB type). Although the most important area for shape memory starts from the single phase $B2$ TiZrHfCoNiCu equiatomic composition and spreads to the ($B2$ + $B19'$) area including it, information on neighbouring areas is also interesting as it might give a hint what kind of precipitation can be expected and even used. Once the phase composition was clarified for the as-cast TiZrHfCoNiCu system (Fig. 4), it was also very important to study the evolution of interatomic interaction within the area of interest. This was done with the help of contour mapping for volume per atom, hardness, Young's modulus and melting temperature.

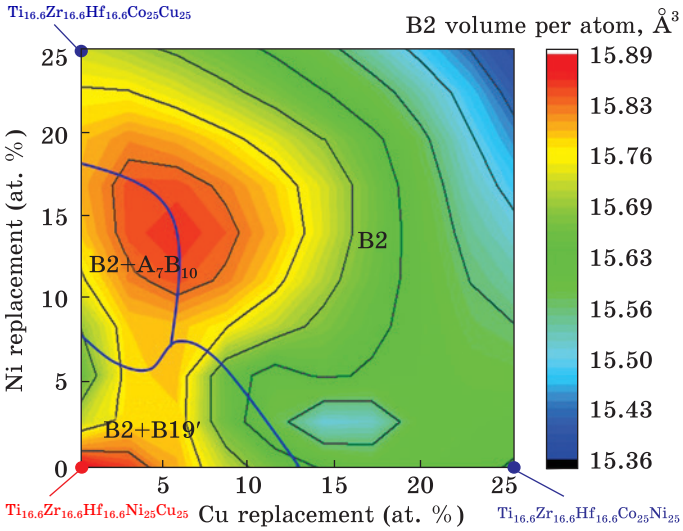

Fig. 5. Contour map for $B2$ volume per atom *versus* Co additions instead of Ni and Cu for $(TiZrHf)_{50}(CoNiCu)_{50}$ alloys; border lines between $B2$, $(B2 + B19')$ and $(B2 + A_7B_{10})$ were taken from the non-equilibrium phase diagram in Fig. 4

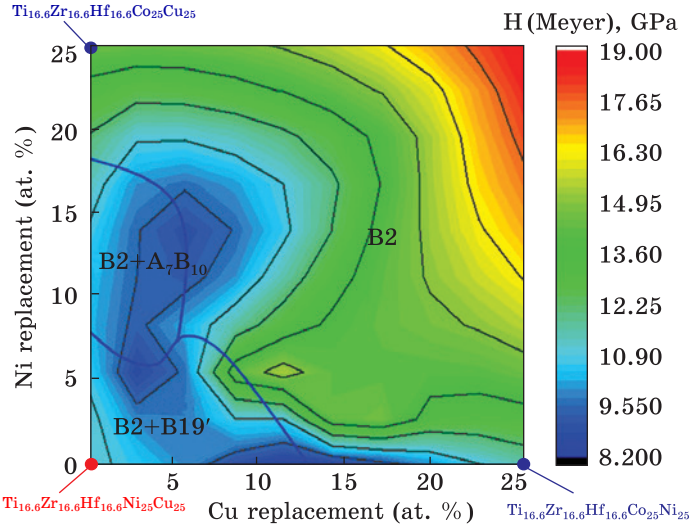

Fig. 6. Contour map for hardness H_{Meyer} *versus* Co additions instead of Ni and Cu for $(TiZrHf)_{50}$ $(CoNiCu)_{50}$ alloys; border lines between $B2$, $(B2 + B19')$ and $(B2 + A_7B_{10})$ were taken from the non-equilibrium phase diagram in Fig. 4

The volume per atom for the $B2$ phase representing average bond length is shown in Fig. 5 depending upon the concentration of Co replacing Ni and Cu. It can be seen that the smallest volume per atom (15.36 Å^3) is observed for $Ti_{16.67}Zr_{16.67}Hf_{16.67}Co_{50}$ indicating the strongest interatomic interaction. The decrease in Co concentration leads to a wide plateau (volume per atom between 15.6 and 15.7 Å^3) that ranges from $Ti_{16.67}Zr_{16.67}Hf_{16.67}Ni_{50}$ to $Ti_{16.67}Zr_{16.67}Hf_{16.67}Cu_{50}$. Beyond that plateau two distinctive peaks in volume per atom are visible. Both peaks are almost fitting to the $(B2 + B19')$ and $(B2 + A_7B_{10})$ areas (Fig. 5) indicating that the $B2$ phase becomes structurally unstable.

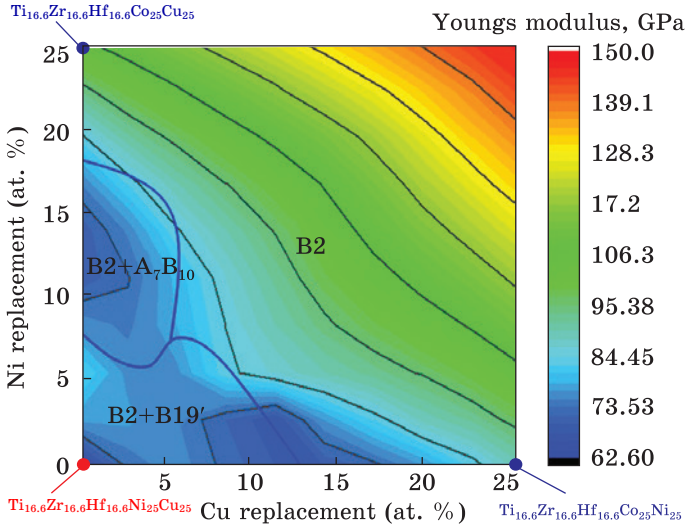

Fig. 7. Contour map for Young's modulus *versus* Co additions instead of Ni and Cu for $(TiZrHf)_{50}$ $(CoNi\ Cu)_{50}$ alloys; border lines between $B2$, $(B2 + B19')$ and $(B2 + A_7B_{10})$ were taken from the non-equilibrium phase diagram in Fig. 4

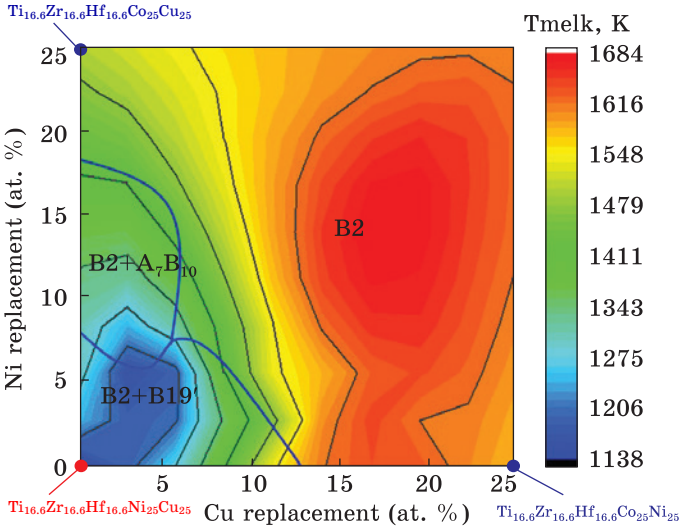

Fig. 8. Contour map for melting temperature Tmelt *versus* Co additions instead of Ni and Cu for $(TiZr\ Hf)_{50}$ $(CoNiCu)_{50}$ alloys; border lines between $B2$, $(B2 + B19')$ and $(B2 + A_7B_{10})$ were taken from the nonequilibrium phase diagram in Fig. 4

Figure 6 represents hardness H_{Meyer} *versus* concentration of Co replacing Ni and Cu in the same way as it was done in Fig. 5. Hardness being a structure sensitive property shows strikingly similar behaviour with almost an anti-correlation if one would compare it to structural parameters such as volume per atom. Indeed, Fig. 6 shows a strong hardness peak at maximum Co content and a subsequent plateau, which shape is very similar to the plateau in Fig. 5. Instead of two peaks in Fig. 5, two minima can be observed in Fig. 6 that are almost fitting the $(B2 + B19')$ and $(B2 + A_7B_{10})$ areas too.

Figures 7 and 8 show the same type of contour maps for Young's modulus and melting temperature T_{melt}. As shown in Fig. 7, Young's modulus, being a structure insensitive property, still exhibits a peak at maximum Co content similarly to hardness and even a plateau, although its shape does not have a resemblance to the plateaus in Fig. 5 and 6. Modulus minima are not exactly fitting the ($B2$ + $B19'$) and ($B2$ + + A_7B_{10}) areas of instability and yet they are covering them in general. The melting temperature has a minimum that fits only the ($B2$ + + $B19'$) area.

The properties sensitive to the interatomic interaction changes show a transient plateau area that separates mostly the stable $B2$ $Ti_{16.67}Zr_{16.67}Hf_{16.67}Co_{50}$ HEI in this system from the $B2$ phase that undergoes a martensitic transformation. It is quite possible that this plateau represents some kind of a pre-martensitic state. This possibility should be explored in more detail as pre-martensitic effects in NiTi definitely play an important role in exploiting their functional properties [39].

Another important issue for the as-cast state $B2$ high-entropy shape-memory intermetallics is related to dendritic liquation. As in this case the number of constituents is between 4 and 6, all of them have different crystallization temperatures and exhibit strong dendritic liquation upon crystallization. Most members of the HESMA development community apply homogenization to eliminate this liquation as it is always done for 'normal' structural or functional materials with one or two principal elements.

Results in [40] show for as-cast $B2$ HEI that dendritic liquation is more pronounced comparing to solid solution HEA, despite the fact that in this case two sublattices have been formed. Comparison of the dendritic liquation in TiZrHfCoNiCu and CoNiCuAlGaIn revealed much stronger separation of the constitutive elements between dendrites and the interdendritic regions. The martensitic crystals grew in specific regions (dendrites in the case of $Ti_{16.67}Zr_{16.67}Hf_{16.67}Co_{10}Ni_{25}Cu_{15}$) and did not penetrate neighbouring ones despite the absence of any clear boundary between the dendrites and the interdendritic regions as it is clearly visible in Fig. 9. The arrowed line in Fig. 9 marks the position, which was used to record EDX line scan data. The results obtained along this line are shown in Fig. 10. It can be seen that the atomic size difference (lattice distortion) is indeed lower in the interdendritic regions and is higher in the dendrite implying that the interatomic interaction is increased. If the composition changes would govern martensite formation, then the Co concentration should be lower in the dendrites. Yet, the situation is quite opposite as there is more Co present in the dendrites. Thus, martensite crystals are prevented from entering neighbouring less distorted interdendritic regions due to the drastic change in the interatomic interaction, which is controlling the martensite crystal growth.

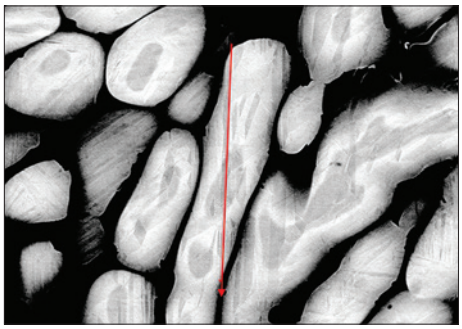

Fig. 9. SEM back-scattered image of $Ti_{16.67}Zr_{16.67}Hf_{16.67}Co_{10}Ni_{25}Cu_{15}$ showing the trace of the EDX line scan

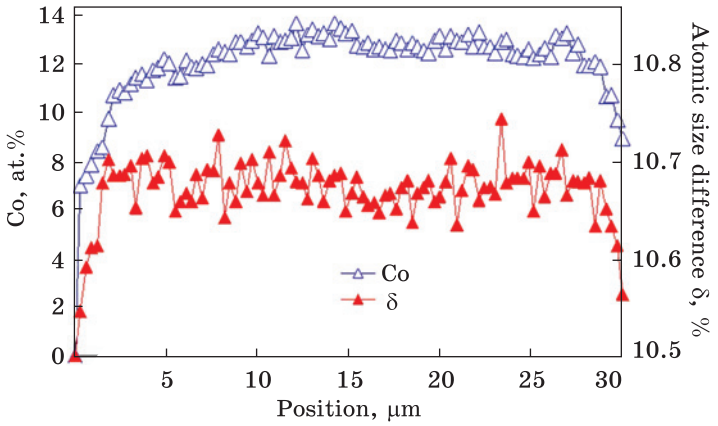

Fig. 10. EDX line scan analysis for as-cast $Ti_{16.67}Zr_{16.67}Hf_{16.67}Co_{10}Ni_{25}Cu_{15}$: Co concentration profile (open triangles) and atomic size difference δ (closed triangles) according to Ref. [18]

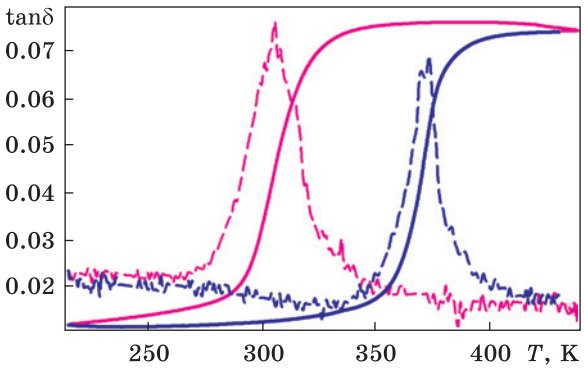

Fig. 11. Dynamic mechanical analysis performed with a Netzsch DMA 24 on as-cast NiTi intermetallic in 3 point bending under a stress of 40 MPa (strain amplitude 0.002, 5 Hz). Solid line — shape-memory behaviour (reversible strain of 0.8%); dashed line — loss factor tanδ

The observed behaviour indicates that shear associated with martensite crystals cannot breach the barrier where the interatomic interaction undergoes drastic change. As the barrier appears to be free from defects, this indicates that shear, associated with dislocations (full or partial) or twins will not be allowed to propagate through this area as well. Such a phenomenon can help with plastic deformation and fatigue prevention in the case of multi-component high-entropy shape-memory

intermetallics. In other words, dendritic liquation, being the characteristic feature of HEI due to their multiple principal element design, might become a positive tool for enhancement of mechanical and functional properties.

4. Functional Properties of High-Entropy *B*2 Shape-Memory Intermetallics

Coming to the issue of functional properties of high-entropy *B*2 shape-memory intermetallics, it has to be noted that significant progress has been already achieved since the first introduction of HESMA. The review [16] describes in detail how the TiZrHfCoNiCu system evolved due to the combined effort of different research groups. Here it is just briefly noted that the so-called NiTi-like HESMAs were successfully homogenised [41], aged [42], the cocktail effect together with compositional changes was added [43], and varies compositions were to understand the homogeneity range of these intermetallics [44, 45]. In Ref. [42], the authors underlined the importance of high yield strength together with high transformation stress levels because this lead to significant work output. In this sense a real breakthrough has been achieved in [46] as the authors managed to realize nanoprecipitation in $Ti_{35}Hf_{10}Zr5(NiCu)_{50}$ intermetallic that resulted in very high transformation stresses and reversible strains and, consequently, in work output up to 188 J/cm^3.

In the following, another possibility of intermetallic HESMA improvement is addressed. As it was reported in the previous section, dendritic liquation in the as-cast state might prove useful for tailoring the functional properties. An example are the simultaneous shape memory and damping behaviour of as-cast NiTi and as-cast $Ti_{16.67}Zr_{16.67}Hf_{16.67}Co_{10}Ni_{20}Cu_{20}$ high-entropy shape-memory intermetallic, *cf*. Figs. 11 and 12. It can be seen for as-cast NiTi (Fig. 11) that against the background of the strain hysteresis loop with MT temperatures of M_s = 350 K, M_f = = 290 K, A_s = 350 K, A_f = 400 K and complete shape recovery (0.8%) one can see loss factor peaks that reach on cooling (forward MT) tanδ = = 7.6%, while on heating (reverse MT) tanδ = 6.8%. Damping is considered to be high if the loss factor is above 3%, and thus NiTi belongs to the high damping materials even in the as-cast state.

The question arises how the $Ti_{16.67}Zr_{16.67}Hf_{16.67}Co_{10}Ni_{20}Cu_{20}$ high-entropy shape-memory intermetallic would behave in the as-cast state when generating the same amount of reversible shape recovery of 0.8%. To analyse this in 3 point bending it was necessary to apply much higher external stress of 300 MPa. For the as-cast $Ti_{16.67}Zr_{16.67}Hf_{16.67}Co_{10}Ni_{20}Cu_{20}$ high-entropy shape-memory intermetallic, shape memory and damping behaviour are shown in Fig. 12. The MT hysteresis loop in this case

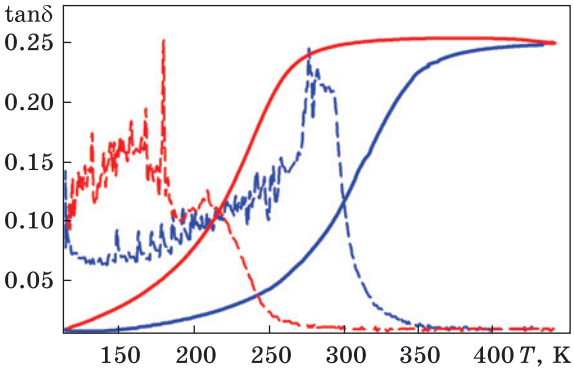

Fig. 12. Dynamic mechanical analysis performed in a Netzsch DMA 24 on as-cast $Ti_{16.67}Zr_{16.67}Hf_{16.67}Co_{10}Ni_{20}Cu_{20}$ high-entropy shape-memory intermetallic in 3 point bending under stress of 300 MPa (strain amplitude 0.002, 5 Hz); solid line — shape memory behaviour (reversible strain of 0.8%); dashed line — loss factor tanδ

is characterised by the following MT temperatures: M_s = 250 K, M_f = 150 K, A_s = 250 K, A_f = 350 K. While MT strain hysteresis loops are quite similar for both intermetallics, the work output for the as-cast $Ti_{16.67}Zr_{16.67}Hf_{16.67}Co_{10}Ni_{20}Cu_{20}$ is 7.5 times higher compared to the as-cast NiTi, because of the higher external stress that generates the same amount of recoverable strain. At the same time, the peaks of the loss factor are much higher for $Ti_{16.67}Zr_{16.67}Hf_{16.67}Co_{10}Ni_{20}Cu_{20}$ during the forward and reverse MT as well. Upon cooling through the forward MT temperature interval tanδ grows up to 12.2% and after a slight decrease it is growing further upon cooling in the martensitic state up to 18% with some loss factor oscillations reaching 24.8% (Fig. 12). Subsequent heating results in a steady loss factor growth from 6.8% up to the A_s temperature and tanδ = 14%. Further heating through the temperature interval of the reverse MT leads to the increase of the loss factor to tanδ = = 24.5%. Such tanδ behaviour for as-cast $Ti_{16.67}Zr_{16.67}Hf_{16.67}Co_{10}Ni_{20}Cu_{20}$ high-entropy shape-memory intermetallic, especially in the martensitic state below M_f can be related to the interaction of the martensite crystals, their internal structure and microstructural elements of the dendritic liquation, which plays a positive role here. NiTi does not have such a microstructural component as liquation, and thus exhibits much lower damping.

5. Conclusions

High-entropy multiple principal element shape memory intermetallics have undergone significant development through composition modifications of the initial TiZrHfCoNiCu system. Thermal treatments can be used to tune their superior shape recovery, superelasticity and work output.

Crystal structure design of high entropy shape-memory intermetallics requires well-directed construction of the sublattices that are characteristic for the *B*2 derivative multi-element intermetallic structure.

The latter belongs to the triclinic syngony and martensite transformation from triclinically distorted $B2$ austenite phase takes place into the triclinically distorted $B19'$ martensite.

In the high-entropy TiZrHfCoNiCu intermetallic compounds two types of interatomic interaction of A–B and B–B type (A = Ti, Zr, Hf; B = Co, Ni, Cu) can be considered as the main reason for the structural instability resulting in a martensitic transformation. Such instability as well as plastic deformation is controlled by the triclinically distorted lattice within the TiZrHfCoNiCu system.

There is a need to develop an approach that will allow a knowledgeable control of the existing phase stabilities, their homogeneity range, lattice distortion, cocktail effect through deliberate manipulation of the interatomic interaction in triclinic lattices.

It is necessary to search for novel intermetallic prototypes that might develop an inclination towards martensitic transformation and shape memory due to the multiple principal element concept. In this context, dendritic liquation appears to be an additional viable route.

Acknowledgements. Financial support by the fundamental Project of the National Academy of Sciences of Ukraine (project number 0123U101764) is gratefully acknowledged. Funding by the Deutsche Forschungsgemeinschaft (DFG) for project number 388671975 in SPP 2006 313773923 is also gratefully acknowledged

REFERENCES

1. J.W. Yeh, S.K. Chen, S.G. Lin, J.Y. Gan, T.S. Chin, T.T. Shun, C.H. Tsau, and S.Y. Chang, *Adv. Eng. Mater.*, **6**: 299–303 (2004); https://doi.org/10.1002/adem.200300567
2. Y. Zhang, T.T. Zuo, Z. Nang, M.C. Cao, K.A. Dahmen, P.K. Liaw, and Z.P. Lu, *Prog. Mater. Sci.*, **61**: 1–93 (2014); https://doi.org/10.1016/j.pmatsci.2013.10.001
3. B.S. Murty, J.-W. Yeh, and S. Ranganathan, *High Entropy Alloys* (Amsterdam, The Netherlands–Oxford, UK: Elsevier Science & Technology–Butterworth-Heinemann Ltd.: 2014), p. 204.
4. B. Cantor, *Entropy*, **16**: 4749–4768 (2014); https://doi.org/10.3390/e16094749
5. Y.F. Ye, Q. Wang, J. Lu, C.T. Liu, and Y. Yang, *Mater. Today*, **19**: 349–362 (2016); https://doi.org/10.1016/j.mattod.2015.11.026
6. V.F. Gorban', N.A. Krapivka, and S.A. Firstov, *Phys. Met. Metallogr.*, **118**: 970–981 (2017); https://doi.org/10.1134/S0031918X17080051
7. O.N. Senkov, J.M. Scott, S.V. Senkova, D.B. Miracle, and C.F. Woodward, *J. Alloys Compd.*, **509**: 6043–6048 (2011); https://doi.org/10.1016/j.jallcom.2011.02.171
8. S.A. Firstov, T.G. Rogul', N.A. Krapivka, S.S. Ponomarev, V.N. Tkach, V.V. Kovylyaev, V.F. Gorban', and M.V. Karpets, *Russ. Metall.*, **2014**: 285–292 (2014); https://doi.org/10.1134/S0036029514040028

9. G.S. Firstov, J. Van Humbeeck, and Y.N. Koval, *Mater. Sci. Eng. A*, **378**: 2–10 (2004);
https://doi.org/10.1016/j.msea.2003.10.324
10. G.S. Firstov, J. Van Humbeeck, and Y.N. Koval, *J. Intel. Mater. Sys. Struct.*, **17**: 1041–1047 (2006);
https://doi.org/10.1177/1045389X06063922
11. J. Ma, I. Karaman, and R.D. Noebe, *Int. Mater. Rev.*, **55**: 257–315 (2010);
https://doi.org/10.1179/095066010X12646898728363
12. T. Niendorf, P. Krooß, E. Batyrsina, A. Paulsen, Y. Motemani, A. Ludwig, P. Buenconsejo, J. Frenzel, G. Eggeler, and H.J. Maier, *Mater. Sci. Eng. A*, **620**: 359–366 (2015);
https://doi.org/10.1016/j.msea.2014.10.038
13. G. Firstov, Y. Koval, J. Van Humbeeck, A. Timoshevskii, T. Kosorukova, and P. Verhovlyuk, *Shape Memory Alloys: Properties, Technologies, Opportunities* (Eds. N. Resnina and V. Rubanik) (Zurich, Switzerland: Trans. Tech. Publications Inc.: 2015), pp. 207–232;
https://doi.org/10.4028/www.scientific.net/MSFo.81-82.207
14. G.S. Firstov, T.A. Kosorukova, Yu.N. Koval, and V.V. Odnosum, *Mater. Today Proc.*, **2**: S499–S504 (2015);
https://doi.org/10.1016/j.matpr.2015.07.335
15. G.S. Firstov, T.A. Kosorukova, Y.N. Koval, and P.A. Verhovlyuk, *Shape Memory and Superelasticity*, **1**, No. 4: 400–407 (2015);
https://doi.org/10.1007/s40830-015-0039-7
16. G. Fu, X. Liu, X. Yi, S. Zhang, X. Cao, X. Meng, Z. Gao, and H. Wang, *Metals* **13**: 1279 (2023);
https://doi.org/10.3390/met13071279
17. J.I. Lee, K. Tsuchiya, W. Tasaki *et al.*, *Sci. Rep.*, **9**: 13140 (2019).
https://doi.org/10.1038/s41598-019-49529-8
18. S. Guo and C.T. Liu, *Progress in Natural Science: Materials International*, **21**, No. 6: 433–446 (2011);
https://doi.org/10.1016/S1002-0071(12)60080-X
19. A. Sato, Y. Yamaji, and T. Mori, *Acta metallurgica*, **34**: 287–294 (1986);
https://doi.org/10.1016/0001-6160(86)90199-9
20. Q. Gu, J. Van Humbeeck, and L. Delaey, *Journal de Physique IV. Proceedings*, **04**, No. C3: 135–144 (1994);
https://doi.org/10.1051/jp4:1994319
21. I. Ferretto, D. Kim, W.J. Lee, E. Hosseini, N.M. della Ventura, A. Sharma, C. Sofras, J. Capek, E. Polatidis, and C. Leinenbach, *Materials & Design* **229**: 111928 (2023);
https://doi.org/10.1016/j.matdes.2023.111928
22. Q. Liao, T. Jing, Y. Wang, H. Peng, and Y. Wen, *J. Alloys Compd.*, **926**: 166803 (2022);
https://doi.org/10.1016/j.jallcom.2022.166803
23. L. Wang, C. Fu, Y. Wu, R. Li, X. Hui, and Y. Wang, *Scripta Materialia*, **162**: 112–117 (2019);
https://doi.org/10.1016/j.scriptamat.2018.10.035
24. J. Fu, A. Yamamoto, H.Y. Kim, H. Hosoda, and S. Miyazaki, *Acta Biomaterialia*, **17**: 56–67 (2015);
https://doi.org/10.1016/j.actbio.2015.02.001
25. G. Firstov, A. Timoshevski, T. Kosorukova, Y. Koval, Y. Matviychuk, and P. Verhovlyuk, *MATEC Web Conf.*, **33**: 06006 (2015);

https://doi.org/10.1051/matecconf/20153306006
26. P. Villars and S. Iwata, *Chemistry of Metals and Alloys*, **6**: 81–108 (2013); https://doi.org/10.30970/cma6.0269
27. S. Guo, Q. Hu, Chun Ng, and C.T. Liu, *Intermetallics*, **41**: 96–103 (2013); https://doi.org/10.1016/j.intermet.2013.05.002
28. B.S. Murty, J.-W. Yeh, S. Ranganathan, and P.P. Bhattacharje, *High Entropy Alloys. Second Edition* (Amsterdam, The Netherlands–Oxford, UK: Elsevier–Cambridge, US: 2019), p. 363.
29. H. Wang, Q.-F. He, and Y. Yang, *Rare Met.*, **41**, No. 6: 1989–2001 (2022); https://doi.org/10.1007/s12598-021-01926-7
30. Yu.N. Koval, G.S. Firstov, J.V. Humbeeck, L. Delaey, and W.J. Jang, *J. Phys. IV*, **5**, No. C8: 1103–1108 (1995); https://doi.org/10.1051/jp4/1995581103
31. Y.N. Koval, G.S. Firstov, and A.V. Kotko, *Scripta Metallurgica et Materialia* **27**, No. 11: 1611–1616 (1992); https://doi.org/10.1016/0956-716X(92)90153-6
32. G.S. Firstov, A.N. Timoshevski, T.A. Kosorukova, and Yu.N. Koval (to be published).
33. https://luttero.github.io/maud
34. G. Firstov, A. Timoshevski, Yu. Koval, S. Yablonovski, and J. Van Humbeeck, *Materials Science Forum*, **738–739**: 15 (2013); https://doi.org/10.4028/www.scientific.net/MSF.738-739.15
35. G. Firstov, Yu. Koval, A. Timoshevski, S. Yablonovski, and J. Van Humbeeck, *Chemistry of Metals and Alloys*, **6**: 205–208 (2013); https://doi.org/10.30970/cma6.0277
36. S. San, S. Hasan, P. Adhikari, and W.-Y. Ching, *Metals*, **13**: 1953 (2023); https://doi.org/10.3390/met13121953
37. G. Gerstein, G.S. Firstov, T.A. Kosorukova, Y.N. Koval, and H.J. Maier, *Shape Mem. Superelasticity*, **4**: 360–368 (2018); https://doi.org/10.1007/s40830-018-0180-1
38. T.A. Kosorukova, G. Gerstein, Y.N. Koval, H.J. Maier, and G.S. Firstov (to be published).
39. K. Otsuka and X. Ren, *Progress in Materials Science*, **50**: 511–678 (2005); https://doi.org/10.1016/j.pmatsci.2004.10.001
40. T. Kosorukova, G. Gerstein, V.V. Odnosum, Y.N. Koval, H.J. Maier, and G.S. Firstov, *Materials*, **12**: 4227 (2019); https://doi.org/10.3390/ma12244227
41. C.-H. Chen and Y.-J. Chen, *Scr. Mater.*, **162**: 185–189 (2019); https://doi.org/10.1016/j.scriptamat.2018.11.023
42. J. Yaacoub, W. Abuzaid, F. Brenne, and H. Sehitoglu, *Scripta Materialia*, **186**: 43–47 (2020); https://doi.org/10.1016/j.scriptamat.2020.04.017
43. I.U. Rehman, S. Li, and T.-H. Nam, *J. Alloys Compd.*, **884**: 161108 (2021); https://doi.org/10.1016/j.jallcom.2021.161108
44. S. Li, D. Cong, Z. Chen, S. Li, C. Song, Y. Cao, Z. Nie, and Y. Wang, *Mater. Res. Lett.*, **9**: 263–269 (2021); https://doi.org/10.1080/21663831.2021.1893233
45. S. Li, D. Cong, X. Sun, Y. Zhang, Z. Chen, Z. Nie, R. Li, F. Li, Y. Ren, and Y. Wang, *Mater. Res. Lett.*, **7**: 482–489 (2019); https://doi.org/10.1080/21663831.2019.1659436
46. G. Zhao, H. Zou, D. Fang, C. Huang, Y. Ye, and X. Ye, *J. Alloys Compd.*, **965**:

171504 (2023);
https://doi.org/10.1016/j.jallcom.2023.171504

Received 01.12.2023;
in final version, 12.12.2023

Г.С. Фірстов[1], *Ю.М. Коваль*[1], *В.С. Філатова*[1],
В.В. Односум[1], *Г. Герштайн*[2], *Г.Ю. Майєр*[2]

[1] Інститут металофізики ім. Г.В. Курдюмова НАН України,
бульв. Академіка Вернадського, 36; 03142 Київ, Україна

[2] Інститут матеріялознавства Університету ім. Ляйбніца у Ганновері,
В університеті 2; 30823 Гарбзен, Німеччина

РОЗРОБКА ВИСОКОЕНТРОПІЙНИХ СТОПІВ З ПАМ'ЯТТЮ ФОРМИ: СТРУКТУРА ТА ВЛАСТИВОСТІ

Серед функціональних матеріялів особливе місце займають стопи з пам'яттю форми. Після їх відкриття ці стопи привернули велику увагу через можливість відновлення значних величин деформації за певних умов температура–напруження завдяки мартенситному бездифузійному фазовому перетворенню, яке відбувається у процесі. Вдалося використати не тільки так звану «пам'ять форми», але також надпружність і високу демпфувальну здатність. Протягом багатьох років було подано понад 10 000 патентів на стопи з пам'яттю форми, які оцінювали не тільки можливість використовувати перетворення енергії для забезпечення зворотнього зв'язку зі зміною незалежних термодинамічних параметрів (температури, напруження, тиску, електричного або магнетного поля тощо), але також і значний обсяг виконуваної роботи. Застосування варіювалися від різних ґаджетів до автомобільної й аерокосмічної промисловостей, машинобудування, цивільного будівництва тощо. На жаль, структурна та функціональна втома обмежила успішне бізнес-застосування щодо медичного сектора стопом нітинол з пам'яттю форми (різні імплантати, стенти, серцево-судинні клапани та ін.). Нові високоентропійні стопи з пам'яттю форми можна розглядати як засіб подолання проблеми втоми наявних промислових стопів з пам'яттю форми завдяки їхній специфічній структурі, яка забезпечує чудову стійкість до незворотньої пластичної деформації.

Ключові слова: високоентропійні стопи з пам'яттю форми, мартенситне перетворення, структура, інтерметалеві сполуки з багатоелементною основою, механічні властивості, пам'ять форми та пов'язані явища.